An Input Current Feedback Method to Mitigate the DC-Side Low-Frequency Ripple Current in a Single-Phase Boost Inverter

Damith B. Wickramasinghe Abeywardana, *Student Member, IEEE*, Branislav Hredzak, *Senior Member, IEEE*, and Vassilios G. Agelidis, *Senior Member, IEEE*

***Abstract*—A boost DC/AC converter is popular in AC line-integrated energy storage systems (ESSs) based on low-voltage DC sources such as battery, fuel cell, or supercapacitor. The direct DC/AC power conversion in the boost inverter introduces a second-order harmonic ripple current at the DC side of the boost converter, which leads to internal heating of the energy storage devices and degradation of their lifetime. In this paper, a novel current feedback method is proposed to mitigate the second-order harmonic current component at the DC side. The proposed method is able to significantly reduce the second-order harmonic component in the DC-side current of the boost inverter without increasing other harmonic components. Performance of the proposed method is validated on a single-phase grid-connected DC/AC boost inverter-based battery ESS experimental prototype.**

***Index Terms*—Battery, boost inverter, fuel cell, second-order harmonic ripple current, supercapacitor.**

I. Introduction

GROWING popularity in distributed power generation evokes the necessity of single-phase grid-connected energy storage systems (ESSs) in the distribution network [1]–[3]. Most of the well-established energy storage technologies such as batteries, fuel cells, and supercapacitors are DC energy storage technologies which require intermediate power converters for single-phase grid integration. The grid interfacing power converters have to step-up the input DC voltage while converting DC power to AC power. Two main kinds of DC/AC power converter structures can be identified: DC-link-based [4] and direct AC line-integrated power converter structures [1]. The boost inverter topology is a direct AC line-integrated power converter structure, which enables the grid integration of low-voltage DC energy storage technologies by providing the required boosting and inversion functions in a single power conversion stage [5], [6].

Due to the single-stage DC-to-AC power conversion, a second-order harmonic current component appears at the DC side of the boost inverter, and hence, the DC ESS has to withstand the low-frequency ripple current. Adverse effects of such a current ripple on the DC ESSs were reported in the technical literature. The effects of low-frequency ripple current on the fuel cell systems were extensively analyzed in [7] and [8] and reported a significant increment in fuel cell losses, which leads to fuel wastage and noticeable reduction in the fuel cell lifetime. Hysteresis relationship between the fuel cell voltage and current and associated losses were analyzed in [8]. Moreover, the authors in [9] reported a significant degradation of available capacity of the fuel cell due to the ripple current. authors in [10] showed that the presence of low-frequency ripple current could increase the internal heating of a lead-acid battery, which resulted in a considerable reduction in its lifetime. Moreover, the charge/discharge microcycles associated with the ripple current also contribute to the battery degradation. Likewise, in [11], the authors reported a temperature rise in a lithium iron phosphate battery due to the low-frequency ripple current. Recently, supercapacitor-based hybrid ESSs have become popular due to their high power capability and extended cycle life [12]–[14]. However, it is shown in [15] that a continuous ripple current could lead to overheating in a supercapacitor, which eventually leads to a deterioration of its lifetime.

Prolonging lifetime of ESS components is a vital aspect of an economical ESS, and hence, numerous ripple current reduction techniques have been proposed for the single-phase boost inverter topology [16]–[20]. Two main types of ripple current reduction methods can be identified in the technical literature, namely passive [16], [17] and active [18]–[20] ripple current reduction methods. In active methods, ripple current reduction is achieved by introducing a control or modulation scheme, while in passive methods, a separate energy storage element is attached to the converter to supply the required ripple current component. In [16] and [17], the authors introduced a separate battery for the second-order harmonic ripple compensation in a boost inverter-based fuel cell ESS. Despite the reduction of fuel wastage and increase in fuel cell lifetime, battery has to suffer the ripple current component, which eventually reduces the lifetime of the battery. Moreover, additional hardware requirement lowers the attractiveness of such a system. Active ripple current reduction methods are attractive over the passive methods, due to its ripple reduction ability without incurring additional hardware. A waveform control method has been proposed in [18] for a boost inverter-based ESS. The method calculated the required output capacitor reference voltage signal such that the ripple current component in the DC side was theoretically eliminated.

Manuscript received March 31, 2015; revised June 12, 2015 and August 19, 2015; accepted August 20, 2015. Date of publication August 26, 2015; date of current version January 7, 2016. Recommended for publication by Associate Editor C. Tse.

The authors are with the School of Electrical Engineering and Telecommunications, The University of New South Wales, Sydney, N.S.W. 2052, Australia (e-mail: d.wickramasingheabeywardana@student.unsw.edu.au; b.hredzak@unsw.edu.au; vassilios.agelidis@unsw.edu.au).

Color versions of one or more of the figures in this paper are available online at http://ieeexplore.ieee.org.

Digital Object Identifier 10.1109/TPEL.2015.2473170

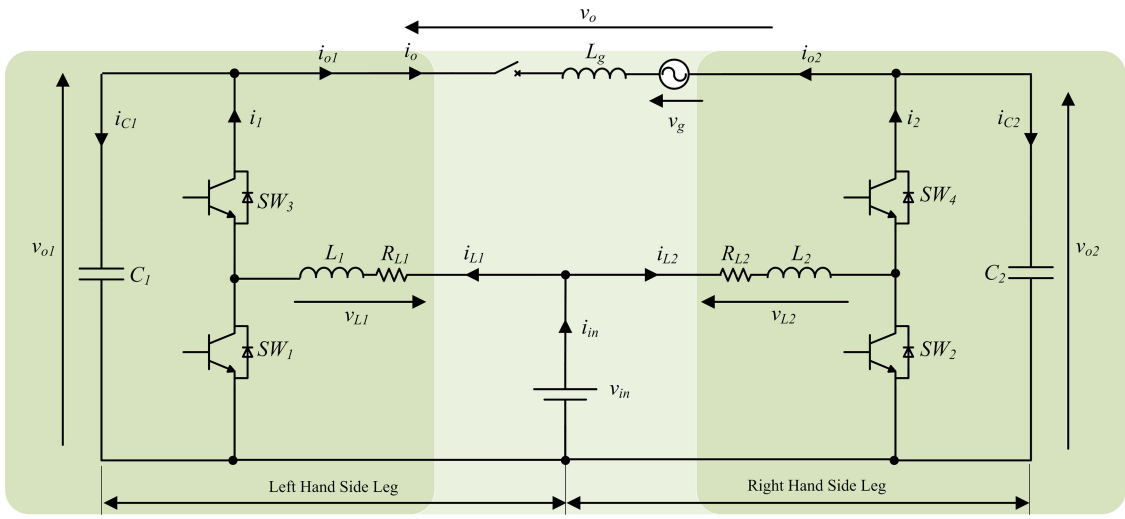

Fig. 1. Single-phase grid-connected battery ESS.

The waveform control technique has been extended to handle active power step changes in [19] and reported the effectiveness of the technique for all output power conditions in [20]. The main disadvantage of the waveform control method is its complexity and possible inaccuracies in output capacitor reference voltage calculation. Moreover, the waveform control method introduces an additional fourth-order harmonic ripple current component at the DC side while reducing the second-order harmonic component. A rule-based controller that generates the required output capacitor reference voltages for the waveform control ripple current reduction method was proposed in [21]. The rule-based controller eliminated possible inaccuracies occurring in the traditional waveform control method due to the capacitor tolerances and was able to achieve better performance. However, the rule-based control method in [21] could not eliminate the additional fourth-order harmonic ripple component introduced by the output capacitor voltage modification.

Numerous active ripple current reduction methods were proposed for various power converter topologies. A ripple current reduction method for a two-stage DC/AC converter was proposed in [22] using a back current gain model. An input current ripple reduction method using a double-loop controller was presented in [23]. A component minimized active power decoupling method was proposed in [24] for an AC/DC power converter as an extension of the active filter-based power decoupling methods proposed in [25] and [26]. These methods were designed for specific power converter topologies, and since the boost inverter has a unique differential operation, the active ripple reduction methods proposed in [22]–[27] cannot be directly applied to the boost inverter topology.

In this paper, a current feedback method is proposed for the second-order harmonic ripple reduction in a boost inverter-based single-phase grid-connected ESS. Effectiveness of the proposed method is theoretically analyzed. In the proposed method, the output capacitor voltage reference signals are modified using the DC-side current feedback signal as opposed to the complex calculations required in the waveform control method. Hence, performance of the proposed method is not affected by the capacitance tolerances of the output capacitors. Moreover, the proposed method is able to reduce the second-order harmonic ripple current at the DC side of the boost inverter without increasing other frequency harmonic components. The method is experimentally verified using a single-phase grid-connected battery ESS prototype.

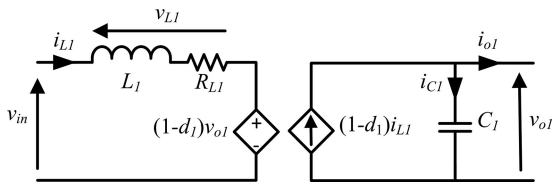

Fig. 2. Average model of the left-hand side boost converter leg.

The remainder of this paper is organized as follows. Operation of the grid-connected boost inverter and the theoretical background of the proposed ripple current reduction method are discussed in Sections II and III, respectively. The boost inverter control system is described in Section IV, and experimental results for the proposed ripple current reduction method are discussed in Section V. Finally, the conclusions of the paper are summarized in Section VI.

II. Operation of Grid-Connected Boost Inverter

A. Overview

The configuration of the boost inverter-based single-phase grid-connected battery ESS is shown in Fig. 1. The converter comprises two boost converter legs: left-hand side boost converter leg (subscript 1) and right-hand side boost converter leg (subscript 2). The boost converter dynamic behavior is described by its average model (see Fig. 2), and the model equations for the left-hand side boost converter leg can be written as

$$v_{\text{in}} - v_{L1} = (1 - d_1)v_{o1} \tag{1}$$

$$i_{C1} + i_{o1} = (1 - d_1)i_{L1} \tag{2}$$

where v_{o1} and i_{C1} are the voltage and current of the capacitor C_1, and v_{L1} and i_{L1} are the voltage and current of the inductor L_1. d_1 denotes the duty cycle time average value of the switch SW_1, while $v_{\rm in}$ is the input voltage to the boost inverter. The output current from the left-hand side boost converter leg denotes as i_{o1}.

The inductor and capacitor differential equations are

$$v_{L1} = R_{L1} i_{L1} + L_1 di_{L1}/dt \tag{3}$$

$$i_{C1} = C_1 dv_{o1}/dt. \tag{4}$$

The differential output voltage of the boost inverter is given by

$$v_o = V_o \sin(\omega t + \delta) \tag{5}$$

where V_o, ω, and δ are the amplitude, frequency, and phase angle of the inverter output voltage, respectively. Voltages across the output capacitors C_1 and C_2 are required to follow independent voltage references $v_{o1,\rm ref}$ and $v_{o2,\rm ref}$ in order to achieve the required differential output voltage v_o

$$v_{o1,\rm ref} = V_d + \frac{V_o}{2}\sin(\omega t + \delta) \tag{6}$$

$$v_{o2,\rm ref} = V_d - \frac{V_o}{2}\sin(\omega t + \delta). \tag{7}$$

The DC shift of the output capacitor voltage V_d has to be selected such that the minimum values of v_{o1} and v_{o2} are always greater than the input voltage.

An interfacing inductor L_g is used to integrate the inverter to a single-phase grid as shown in Fig. 1, where the grid voltage v_g is given by

$$v_g = V_g \sin(\omega t). \tag{8}$$

For small δ values, the active power (P) and the reactive power (Q) exchanged with the grid can be approximated as [28]

$$P \approx \frac{V_g V_o}{2\omega L_g}\delta \tag{9}$$

$$Q \approx \frac{V_g(V_o - V_g)}{2\omega L_g}. \tag{10}$$

Thus, the active and reactive power flow between the inverter and the grid can be achieved by controlling the inverter output voltage amplitude V_o and phase angle δ with respect to the grid voltage [28], [29].

B. Second-Order Harmonic Input Ripple Current Component in the Boost Inverter

The inverter output current i_o is given by

$$i_o = I_o \sin(\omega t + \alpha) \tag{11}$$

where α is the phase angle of the inverter output current with respect to the grid voltage.

Using (4)–(6) and (11)

$$i_1 = I_o \sin(\omega t + \alpha) + C\omega \frac{V_o}{2}\cos(\omega t + \delta) \tag{12}$$

where $C = C_1 = C_2$.

Similarly

$$i_2 = -I_o \sin(\omega t + \alpha) - C\omega \frac{V_o}{2}\cos(\omega t + \delta). \tag{13}$$

The total input current to the boost inverter is given by

$$i_{\rm in} = i_1 \frac{v_{o1}}{v_{\rm in}} + i_2 \frac{v_{o2}}{v_{\rm in}} \tag{14}$$

which can be rewritten using (12) and (13) as

$$i_{\rm in} = \frac{1}{v_{\rm in}}\left[\frac{V_o I_o}{2}\cos(\alpha - \delta) + \frac{V_o}{2}\sqrt{\left[I_o^2 + \frac{C^2\omega^2 V_o^2}{4} + V_o I_o C\omega \sin(\alpha - \delta)\right]}.\cos(2\omega t - \theta)\right] \tag{15}$$

where

$$\cos\theta = \frac{-I_o \cos(\alpha + \delta) + \frac{C\omega V_o \sin(2\delta)}{2}}{\sqrt{\left[I_o^2 + \frac{C^2\omega^2 V_o^2}{4} + V_o I_o C\omega \sin(\alpha - \delta)\right]}}.$$

From (15), the boost inverter total input current contains a DC component which corresponds to the inverter output power and the second-order harmonic current component which depends on the inverter output current amplitude I_o and phase angle α.

III. Current Feedback-Based Second-Order Harmonic Input Current Ripple Reduction Method

In this paper, an input current feedback method is proposed to reduce the second-order harmonic input ripple current component. In (15), the boost inverter input current can be rewritten as

$$i_{\rm in} = i_{\rm in,DC} + i_{\rm in,AC} \tag{16}$$

where $i_{\rm in,DC}$ and $i_{\rm in,AC}$ are the DC and AC components of the total input current, respectively.

The output capacitor voltage references $v_{o1,\rm ref}, v_{o2,\rm ref}$ given by (6) and (7) can be modified as (17) and (18), without affecting the inverter differential output voltage

$$v_{o1,\rm ref} = V_d + \frac{V_o}{2}\sin(\omega t + \delta) - K i_{\rm in,AC} \tag{17}$$

$$v_{o2,\rm ref} = V_d - \frac{V_o}{2}\sin(\omega t + \delta) - K i_{\rm in,AC} \tag{18}$$

where K is the feedback gain value (see Fig. 6). Then

$$i_1 = I_o \sin(\omega t + \alpha) + C\omega \frac{V_o}{2}\cos(\omega t + \delta) - CK\frac{di_{\rm in,AC}}{dt} \tag{19}$$

and

$$i_2 = -I_o \sin(\omega t + \alpha) - C\omega \frac{V_o}{2}\cos(\omega t + \delta) - CK\frac{di_{\rm in,AC}}{dt}. \tag{20}$$

Using (14), (17), (18), (19) and (20), a differential equation for the input current AC component $i_{\rm in,AC}$ can be obtained as

$$\frac{di_{\rm in,AC}}{dt} = \frac{v_{\rm in}}{(2V_d CK - 2CK^2 i_{\rm in,AC})}\left(i_{\rm in,AC0} - i_{\rm in,AC}\right) \tag{21}$$

TABLE I
ESS EXPERIMENTAL PROTOTYPE PARAMETERS

Parameter	Value	Parameter	Value
Power converter parameters			
V_o	40 V	f	50 Hz
C_1,C_2	60 uF	L_1,L_2	210 uH
$I_{o,max}$	1A	T_F	0.001
V_d	45 V	f_{sw}	20 kHz
Grid parameters			
V_g	40 V	L_g	20 mH
Voltage control loop parameters			
$K_{p,PR}$	0.1	$K_{i,PR,100Hz}$	6
$K_{i,PR,50Hz}$	4	$\omega_{c,50Hz}$, ω_{c100Hz}	0.5
Current control loop parameters			
$K_{p,PI}$	2.615	$K_{i,PI}$	8.44×10^{-5}
Active and reactive power controller parameters			
$K_{p,PI(active)}$	2×10^{-6}	$K_{p,PI(reactive)}$	1×10^{-5}
$K_{i,PI(active)}$	0.14	$K_{i,PI(reactive)}$	4

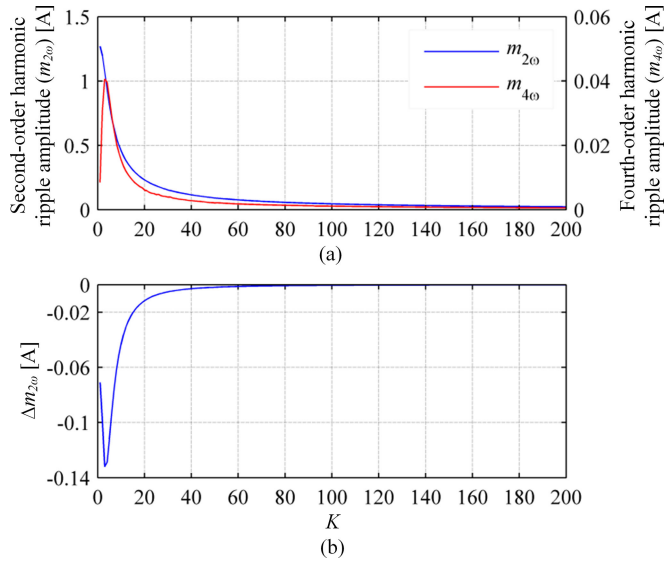

Fig. 3. Numerical solution of the variation of the input current with *K*. (a) Second- and fourth-order harmonic current ripple amplitude. (b) Change in the second-order harmonic ripple amplitude for a unit change in *K*.

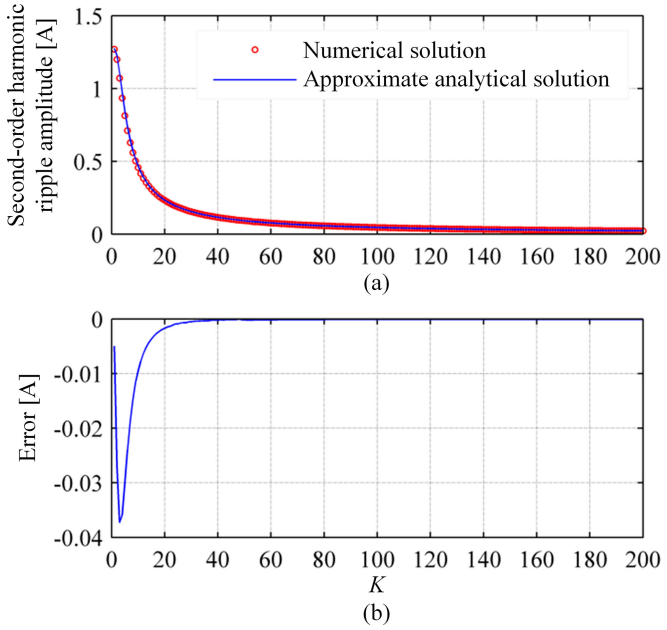

Fig. 4. Comparison of the numerical and approximated analytical solution. (a) Second-order harmonic current ripple amplitude. (b) Error between the numerical and analytical solution.

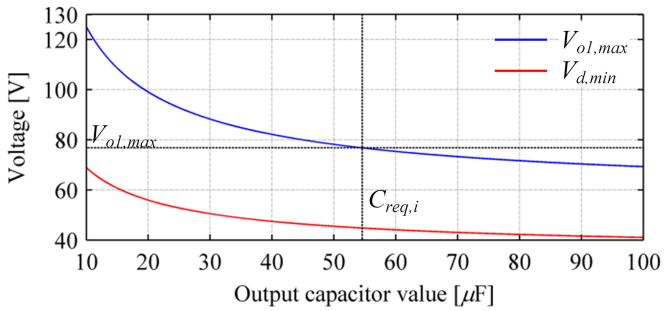

Fig. 5. Relationship between the $V_{o1,\max}$ and $V_{d,\min}$ versus the output capacitor values *C* for the current feedback ripple reduction method.

where

$$i_{\text{in,AC0}} = \frac{V_o}{2v_{\text{in}}}\sqrt{\left[I_o^2 + \frac{C^2\omega^2V_o^2}{4} + V_oI_oC\omega\sin(\alpha-\delta)\right]} \cdot \cos(2\omega t - \theta) \tag{22}$$

corresponds to the AC component of the input current i_{in} given in (15) for the unmodified output capacitor reference voltages (6) and (7).

Before finding an analytical solution, first, a numerical solution of the differential equation (21) is found using MATLAB for a sample case of inverter supplying 15 W active power and 10 VAr reactive power to the grid and considering experimental prototype parameters summarized in Table I. Fig. 3(a) illustrates the second-order harmonic component amplitude ($m_{2\omega}$) and the fourth-order harmonic component amplitude ($m_{4\omega}$) of the obtained numerical solution for various values of the feedback gain *K*. From Fig. 3(a), it is evident that the higher the value of the feedback gain *K*, the more significant is the reduction in the second-order as well as the fourth-order harmonic components of the input current. A change in $m_{2\omega}$ for a unit change in *K*, ($\Delta m_{2\omega}$), is shown in Fig. 3(b). As *K* becomes larger, the change in $m_{2\omega}$ becomes smaller. Using this result, the required minimum value for *K* can be found such that

$$|\Delta m_{2\omega}| \le \Delta m_{2\omega,\max} \tag{23}$$

where $\Delta m_{2\omega,\max}$ is a predetermined value of the maximum allowed change in $m_{2\omega}$ for a unit change in *K* for all possible output power conditions. Then, for the selected maximum change in the second-order harmonic ripple amplitude for a unit change in *K*, $\Delta m_{2\omega,\max}$, the bounds on *K* are given by

$$0 < K \le [K]\left(\Delta m_{2\omega,\max} \ge |\Delta m_{2\omega}|\right). \tag{24}$$

Now, to obtain an analytical solution of the second-order harmonic input current amplitude $m_{2\omega}$, it is assumed that the

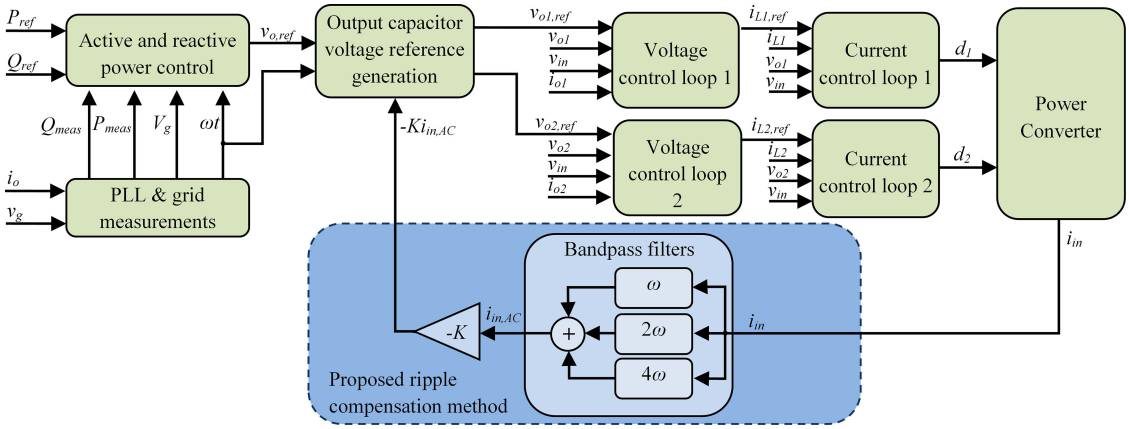

Fig. 6. Overall block diagram of the control system.

steady-state input current AC component with the modified output capacitor voltage references is

$$i_{\mathrm{in,AC}} = m_{2\omega}\cos(2\omega t + \theta_{\omega 2}) + m_{4\omega}\cos(4\omega t + \theta_{\omega 4}). \quad (25)$$

The AC component input current differential equation (21) can be rewritten as

$$2V_d CK\frac{di_{\mathrm{in,AC}}}{dt} - 2CK^2 i_{\mathrm{in,AC}}\frac{di_{\mathrm{in,AC}}}{dt} + v_{\mathrm{in}} i_{\mathrm{in,AC}} = v_{\mathrm{in}} i_{\mathrm{in,AC0}}. \quad (26)$$

After substituting (25) into (26) and simplifying, (26) is obtained

$$-4V_d CK\omega m_{2\omega}\sin(2\omega t + \theta_{2\omega}) + 2CK^2\omega m_{2\omega} m_{4\omega} \sin(2\omega t + \theta_{4\omega} - \theta_{2\omega}) + v_{\mathrm{in}} m_{2\omega}\cos(2\omega t + \theta_{2\omega}) = v_{\mathrm{in}} i_{\mathrm{in,AC0}}. \quad (27)$$

Considering that the product $m_{2\omega}m_{4\omega} \approx 0$, since $m_{2\omega}$ and $m_{4\omega}$ are very small when K is high, the magnitude of the second-order harmonic component in (27) can be found as

$$m_{2\omega} = \frac{v_{\mathrm{in}}\,|i_{\mathrm{in,AC0}}|}{\sqrt{(-4V_d CK\omega)^2 + v_{\mathrm{in}}^2}}. \quad (28)$$

Fig. 4(a) compares the obtained analytical solution (28) with the numerical solution found using MATLAB when the inverter delivers 15 W, 10 VAr to the grid. The error between the numerical and the analytical solution ($m_{2\omega,\mathrm{numerical}} - m_{2\omega,\mathrm{analytical}}$) is shown in Fig. 4(b) and proves the validity of (28) for higher values of K.

For further evaluation of the proposed method, a ripple reduction factor R is defined as the ratio of $m_{2\omega}$ before and after application of the current feedback method. The ripple reduction factor R can be derived from (28) as

$$R = \frac{\sqrt{(4V_d CK\omega)^2 + v_{\mathrm{in}}^2}}{v_{\mathrm{in}}}. \quad (29)$$

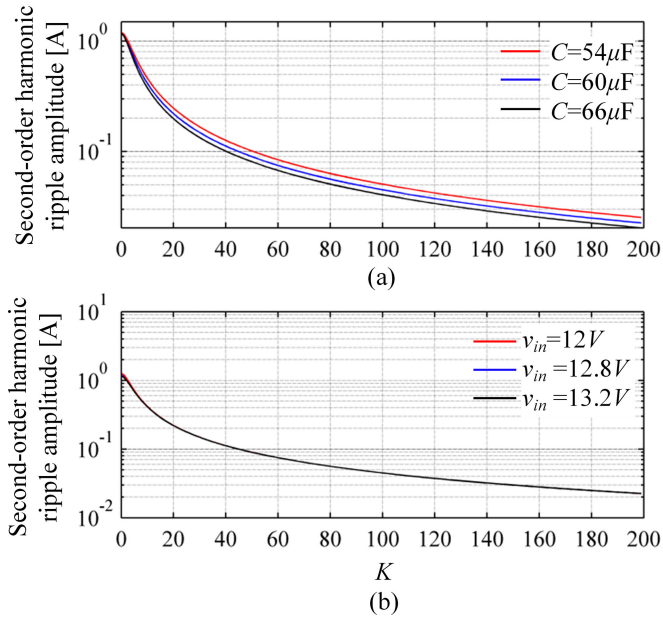

Fig. 7. Illustration of the effect of (a) the output capacitor tolerance and (b) the input voltage variation on the ripple reduction method performance when $P = 15$ W and $Q = 10$ VAr.

To ensure proper operation of the boost inverter, the DC shift of the output capacitor voltage V_d has to meet the condition

$$V_d \geq v_{\mathrm{in}} + \frac{V_o}{2} + \max(Ki_{\mathrm{in,AC}}). \quad (30)$$

According to the numerical solution shown in Fig. 3(a), the second-order harmonic ripple component is the dominant component in the input current compared to the fourth-order harmonic component. Hence, (30) can be rewritten as

$$V_d \geq v_{\mathrm{in}} + \frac{V_o}{2} + \max(Km_{2\omega}). \quad (31)$$

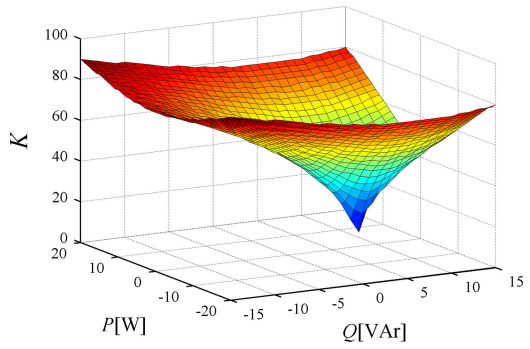

Fig. 8. Illustration of the required feedback gains K to satisfy (23) for each output power condition.

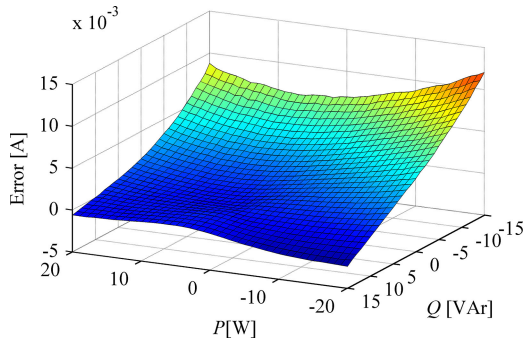

Fig. 9. Error between the numerical solution and the analytical solution for all output power conditions and $K = 100$.

Then, using (28) and assuming large K, (31) can be approximated as

$$V_d \geq v_{\text{in}} + \frac{V_o}{2} + \frac{v_{\text{in}} \max\left(\left|i_{\text{in,AC0}}\right|\right)}{4V_d C\omega} \tag{32}$$

where

$$\max\left(\left|i_{\text{in,AC0}}\right|\right) = \frac{V_o}{2v_{\text{in}}}\sqrt{\left[I_{o,\max}^2 + \frac{C^2\omega^2 V_o^2}{4} + V_o I_{o,\max} C\omega\right]}. \tag{33}$$

Then, the minimum required DC voltage shift V_d for the output capacitor reference voltages can be calculated from

$$V_d \geq V_{d,\min} \tag{34}$$

where

$$V_{d,\min} = \frac{2C\omega\left(V_o + 2v_{\text{in}}\right) + \sqrt{\left[2C\omega\left(V_o + 2v_{\text{in}}\right)\right]^2 + 16C\omega v_{\text{in}} \max\left(\left|i_{\text{in,AC0}}\right|\right)}}{8C\omega}. \tag{35}$$

Then, the maximum output capacitor voltage $V_{o1,\max}$ when $V_d = V_{d,\min}$ is

$$V_{o1,\max} = V_{d,\min} + \frac{V_o}{2} + \frac{v_{\text{in}} \max\left(\left|i_{\text{in,AC0}}\right|\right)}{4V_{d,\min} C\omega}. \tag{36}$$

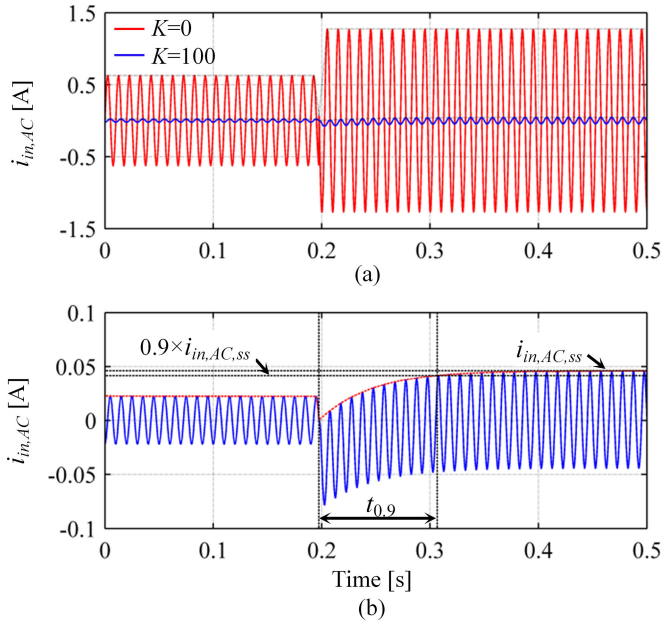

Fig. 10. Dynamic response of the current feedback ripple reduction method for a 15 W, 10 VAr step change. (a) Input current ripple component without ($K = 0$) and with the proposed ripple reduction method ($K = 100$), and (b) input current ripple component when $K = 100$.

TABLE II
COMPARISON OF $t_{0.9}$ (TIME REQUIRED TO REACH 90% OF THE STEADY-STATE VALUE OF THE RIPPLE CURRENT) FOR DIFFERENT OUTPUT POWER STEP CHANGES

P [W]	Q [VAr]	$t_{0.9}$ [s]
20	0	0.1063
−20	0	0.1072
0	15	0.0050
0	−15	0.0080
15	10	0.1100
15	−10	0.0878
−15	10	0.1137
−15	−10	0.0894

The relationship between the $V_{d,\min}$ and $V_{o1,\max}$ versus the output capacitor value C for the experimental prototype parameters given in Table I is illustrated in Fig. 5. The required output capacitor value $C_{\text{req},i}$ can be found as explained in [21]. First, the maximum allowable output capacitor voltage is obtained using the input voltage v_{in} and the maximum gain of the converter legs $G_{\max}$, as $V_{o1,\max} = v_{\text{in}} G_{\max}$. Then, the required output capacitor value $C_{\text{req},i}$ and the minimum DC voltage shift corresponding to $V_{o1,\max}$ can be found from Fig. 5. A detailed comparison of the output capacitor requirement for the boost inverter operation without and with an output capacitor voltage modified ripple reduction method can be found in [21].

IV. DESIGN OF THE BOOST INVERTER CONTROL SYSTEM WITH THE CURRENT FEEDBACK METHOD

The overall block diagram of the grid-connected boost inverter with the proposed ripple current reduction method is

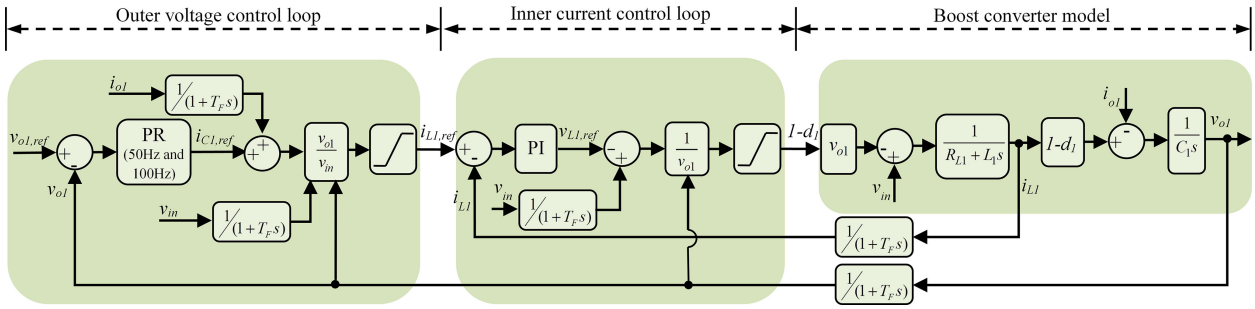

Fig. 11. Outer voltage control loop and inner current control loop for the left-hand side boost converter leg.

shown in Fig. 6. A set of bandpass filters are employed to obtain the AC component of the input current with minimum phase distortion and to block any DC component of the input current in the feedback path.

The maximum gain of the boost converter leg is taken as 6, and hence, the $V_{o1,\max}$ equals 76.8 V. Then, the required output capacitor value for the operation of the boost inverter with the current feedback method is obtained from Fig. 5 as 54.6 μF. The nearest commercially available value of 60 μF was selected for the experimental setup. To observe the effect of the output capacitor tolerance on the ripple reduction performance, (21) was solved for a $\pm 10\%$ variation in the selected capacitance value (60 μF) and the results are illustrated in Fig. 7(a). Similarly, the ripple reduction method performance was evaluated for the battery voltage variation from 12 to 13.2 V and the results are shown in Fig. 7(b). It is evident that the effect of both the output capacitor tolerance and the input voltage variation on the performance of the proposed method is negligible.

The minimum required feedback gains K to satisfy (23) for $\Delta m_{2\omega,\max} = 0.001$ A are calculated for each output power condition. The calculated feedback gains are illustrated in Fig. 8. Then, the value of $K = 100$ is selected to satisfy (23) for all output power conditions. To verify the validity of the approximated analytical solution for the selected K, the error between the numerical solution and the analytical solution for all output power conditions and $K = 100$ is illustrated in Fig. 9. It is evident that the error is negligible.

Dynamic behavior of the proposed current feedback ripple reduction method in response to a power step change can be analyzed using (9)–(11), (21), and (22). Fig. 10 shows the dynamic behavior in response to a power step $P = 15$ W, $Q = 10$ VAr. Fig. 10(a) compares the ripple in the input current without ($K = 0$) and with the proposed ripple reduction method ($K = 100$). In Fig. 10(b), the steady-state peak value of the ripple amplitude after the power step change is defined as $i_{\text{in,AC},ss}$. Then, the time required to reach 90% of the steady-state value $i_{\text{in,AC},ss}$ is taken as $t_{0.9}$. A comparison of the $t_{0.9}$ values for all output power conditions is summarized in Table II and demonstrates that the proposed method is effective in eliminating the ripple current even during the transients.

The boost inverter controller design is explained next. Two double-loop controllers with an inner current and an outer voltage control loop are employed for accurate tracking of the output capacitor voltages $v_{o1,\text{ref}}$ and $v_{o2,\text{ref}}$. Fig. 11 shows the block diagram of the double-loop controller for the left-hand side boost converter leg. A proportional-resonant (PR) controller is employed to enable the accurate voltage reference following. Two resonant components of the PR controller are implemented at 50 and 100 Hz. Inner current control loop is designed based on a proportional-integral (PI) controller. The outer voltage control loops are designed to achieve 400 Hz bandwidth and the inner current control loops are designed with 4 kHz bandwidth. Both control loops are designed to obtain at least 50° phase margin [5], [29].

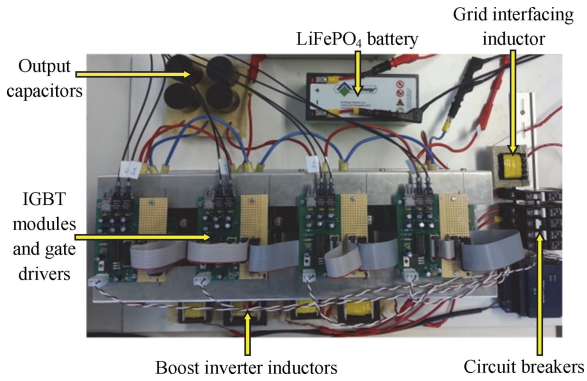

Fig. 12. ESS experimental prototype.

Interleaved operation of the boost inverter proposed in [30] is used to reduce the switching frequency ripple component in the DC-side current.

The grid integration of the inverter is carried out using an interfacing inductor as shown in Fig. 1. The active and reactive power flow between the boost inverter and the grid is achieved by controlling the inverter output voltage amplitude and phase angle with respect to the grid voltage. Two PI controllers are designed using (9) and (10) to control the active and reactive power exchange as shown in [30]. The active and reactive power PI controller parameters are summarized in Table I. For the grid power measurement and the grid synchronization, a second-order generalized integrator-based phase-locked loop is used [31].

V. Experimental Results

The proposed current ripple reduction method for a grid-connected boost inverter was verified using the experimental

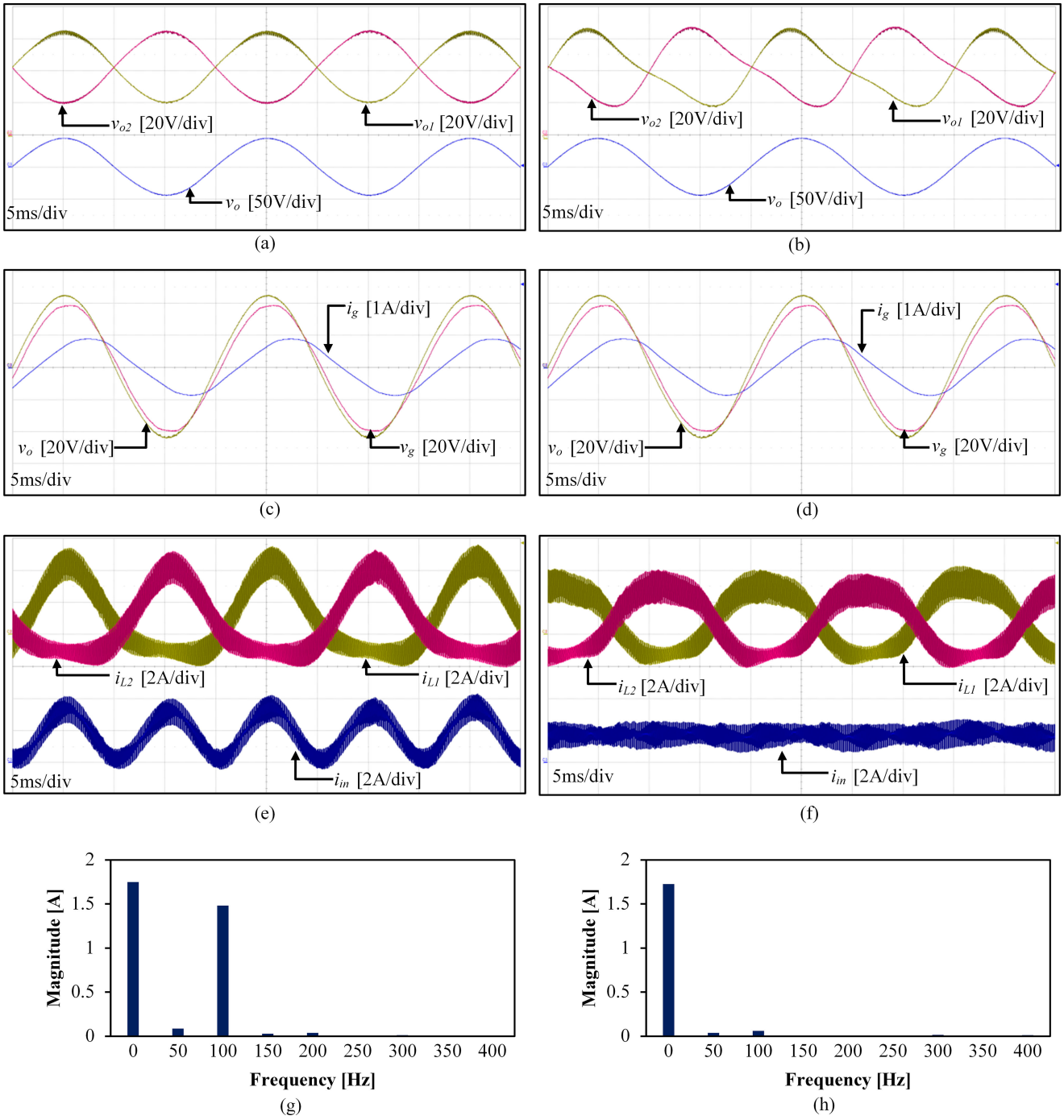

Fig. 13. Experimental results illustrating operation of the battery storage system when delivering 15 W active power and 10 VAr reactive power. (a) Output capacitor voltage waveforms and inverter output voltage without the proposed controller. (b) Output capacitor voltage waveforms and inverter output voltage with the proposed controller. (c) Inverter output voltage, grid voltage, and inverter output current without the proposed controller. (d) Inverter output voltage, grid voltage, and inverter output current with the proposed controller. (e) Inductor currents and total input current of the boost inverter without the proposed controller. (f) Inductor currents and total input current of the boost inverter with the proposed controller. (g) Frequency characteristics of the input current without the proposed controller. (h) Frequency characteristics of the input current with the proposed controller.

setup shown in Fig. 12. Parameters of the boost inverter and controllers are summarized in Table I. A 12.8 V, 6.4 Ah, $LiFePO_4$ battery was used as the input power source to the boost inverter. The boost inverter controllers were implemented on a DSpace DS1006 platform using MATLAB/Simulink. Grid integration of the ESS was achieved through a step-up transformer.

Fig. 13 illustrates operation of the single-phase grid-connected boost inverter with and without the proposed second-order harmonic ripple reduction method when delivering 15 W active and 10 VAr reactive power to the grid. The output capacitor voltage waveforms and the inverter output voltage are shown in Fig. 13(a) and (b) without and with the proposed

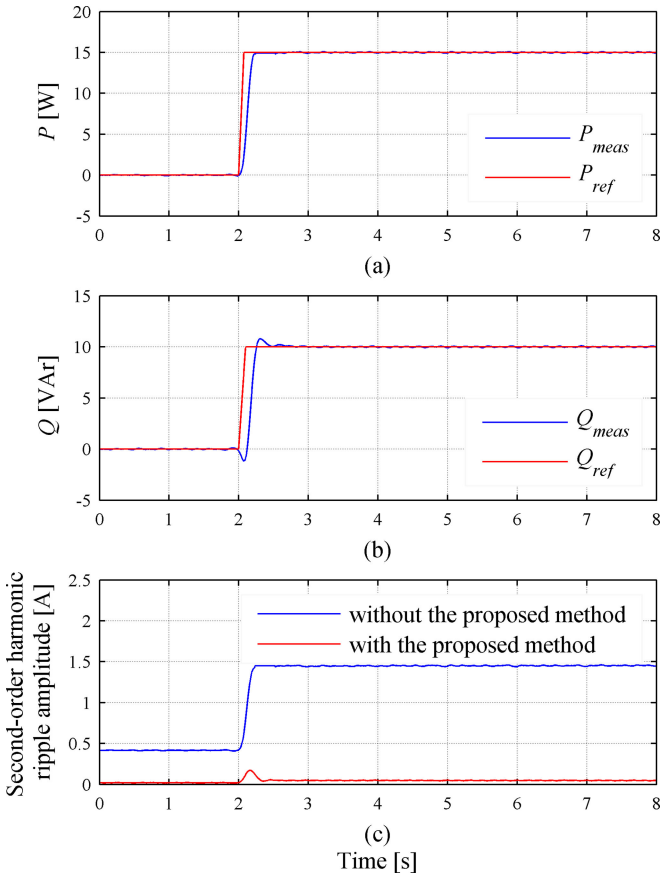

Fig. 14. Experimental results illustrating transient operation of the proposed control system in response to 15 W and 10 VAr power step change. (a) Inverter output active power. (b) Inverter output reactive power. (c) Second-order harmonic ripple amplitude with and without the proposed method.

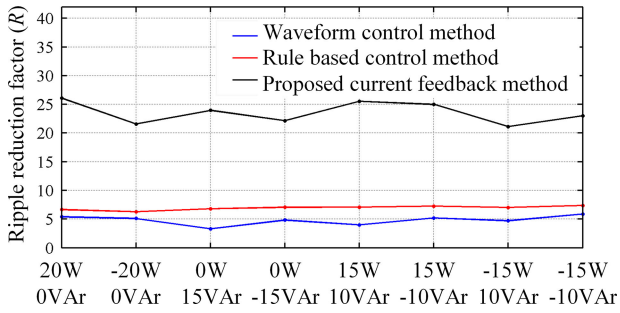

Fig. 15. Comparison of the ripple current reduction using the waveform control method [17], the rule-based control method [20], and the proposed current feedback method ($K = 100$).

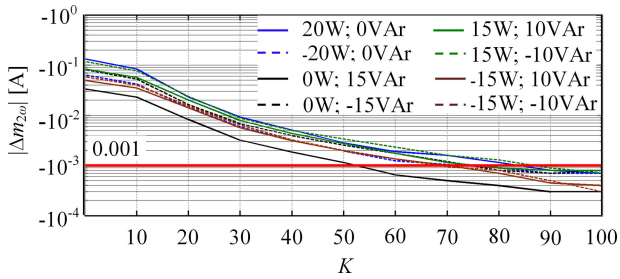

Fig. 16. Experimental results illustrating change in the second-order harmonic ripple current amplitude $|\Delta m_{2\omega}|$ for a unit change in K for all output power conditions.

method, respectively. The inverter output voltage remains unchanged despite the modification of the output capacitor voltages. The operation of the active and reactive power controller is illustrated in Fig. 13(c) and (d). Fig. 13(e) and (f) depicts the inductor current waveforms of the boost converter legs and the total input current to the boost inverter without and with the proposed ripple current reduction method, respectively. The inductor current waveforms modified due to the changes in the output capacitor voltage waveforms and a significant reduction of the input current ripple component can be observed.

The frequency spectrum characteristics of the boost inverter DC-side current with and without the proposed ripple current reduction method are compared in Fig. 13(g) and (h). The second-order harmonic ripple amplitude is reduced from 1.482 to 0.0588 A, achieving approximately 25 times second-order harmonic ripple current reduction. In addition, the proposed method reduced the first-order harmonic current component amplitude from 0.085 to 0.036 A and the fourth-order harmonic current component amplitude from 0.037 to 0.004 A. The frequency spectrum characteristics illustrate the ability of the proposed system to mitigate the second-order harmonic ripple component of the boost inverter input current without increasing other harmonic current components.

Dynamic performance of the proposed ripple current reduction method is shown in Fig. 14. At $t = 2$ s, 15 W active power and 10 VAr reactive power reference step change was applied. Without the proposed method, the second-order harmonic ripple amplitude reaches 1.482 A due to output power step change. However, with the proposed system, the maximum second-order harmonic ripple amplitude during the transient time is 0.172A and reduces to 0.0588A in the steady state. This validates the ability of the proposed method to reduce the second-order harmonic current component even during the active and reactive power transients.

The boost inverter input current ripple reduction achieved using the proposed current feedback method is compared with the waveform control method [18] and the rule-based control method [21] for all the output power conditions in Fig. 15. In order to have a fair comparison, the same experimental setup and control parameters as in [21] were used. It can be observed that the proposed current feedback method is able to reduce the second-order harmonic ripple current more than 20 times for all output power conditions.

The change in the second-order harmonic ripple current amplitude $|\Delta m_{2\omega}|$ for a unit change in K is illustrated for each output power condition in Fig. 16. The result validates that the selection of the feedback gain $K = 100$ results in the change in the second-order harmonic ripple current amplitude $|\Delta m_{2\omega}| < 0.001$ for all output power conditions.

VI. Conclusion

Due to the direct DC/AC power conversion in the conventional boost inverter, a second-order harmonic ripple current appears in the DC side of the converter, and hence, the DC power source connected to the inverter has to handle the ripple current components. Such ripple current can significantly increase the internal heating and losses in the DC power source leading to a reduction in ESS lifetime. In this paper, a novel DC-side current feedback method that reduces the second-order harmonic ripple current without increasing other frequency harmonic components was proposed. Unlike the waveform control methods, the proposed method does not depend on calculations, and hence, its performance is not affected by the capacitance tolerances of the output capacitors. Performance of the proposed method has been experimentally verified using a grid-connected battery ESS prototype and the results have validated its effectiveness in reducing the second-order harmonic ripple current at the DC side of the boost inverter without increasing other frequency harmonic components in both steady-state and transient operation.

References

[1] Q. Hao, Z. Jianhui, L. Jih-Sheng, and Y. Wensong, "A high-efficiency grid-tie battery energy storage system," *IEEE Trans. Power Electron.*, vol. 26, no. 3, pp. 886–896, Mar. 2011.

[2] C. A. Hill, M. C. Such, C. Dongmei, J. Gonzalez, and W. M. Grady, "Battery energy storage for enabling integration of distributed solar power generation," *IEEE Trans. Smart Grid*, vol. 3, no. 2, pp. 850–857, Jun. 2012.

[3] A. Kuperman, U. Levy, J. Goren, A. Zafransky, and A. Savernin, "Battery charger for electric vehicle traction battery switch station," *IEEE Trans. Ind. Electron.*, vol. 60, no. 12, pp. 5391–5399, Dec. 2013.

[4] Z. Haihua, T. Bhattacharya, T. Duong, T. S. T. Siew, and A. M. Khambadkone, "Composite energy storage system involving battery and ultracapacitor with dynamic energy management in microgrid applications," *IEEE Trans. Power Electron.*, vol. 26, no. 3, pp. 923–930, Mar. 2011.

[5] P. Sanchis, A. Ursaea, E. Gubia, and L. Marroyo, "Boost DC-AC inverter: A new control strategy," *IEEE Trans. Power Electron.*, vol. 20, no. 2, pp. 343–353, Mar. 2005.

[6] R. O. Caceres and I. Barbi, "A boost DC-AC converter: Analysis, design, and experimentation," *IEEE Trans. Power Electron.*, vol. 14, no. 1, pp. 134–141, Jan. 1999.

[7] J. Wu, X. Z. Yuan, J. J. Martin, H. Wang, J. Zhang, J. Shen, S. Wu, and W. Merida, "A review of PEM fuel cell durability: Degradation mechanisms and mitigation strategies," *J. Power Sources*, vol. 184, pp. 104–119, Sep. 15, 2008.

[8] R. Ferrero, M. Marracci, and B. Tellini, "Single PEM fuel cell analysis for the evaluation of current ripple effects," *IEEE Trans. Instrum. Meas.*, vol. 62, no. 5, pp. 1058–1064, May 2013.

[9] C. Woojin, P. N. Enjeti, and J. W. Howze, "Development of an equivalent circuit model of a fuel cell to evaluate the effects of inverter ripple current," in *Proc. 19th Annu. IEEE Appl. Power Electron. Conf. Expo.*, 2004, vol. 1, pp. 355–361.

[10] A. J. Ruddell, A. G. Dutton, H. Wenzl, C. Ropeter, D. U. Sauer, J. Merten, C. Orfanogiannis, J.W. Twidell, and P. Vezin, "Analysis of battery current microcycles in autonomous renewable energy systems," *J. Power Sources*, vol. 112, pp. 531–546, Nov. 14, 2002.

[11] S. Bala, T. Tengner, P. Rosenfeld, and F. Delince, "The effect of low frequency current ripple on the performance of a lithium iron phosphate (LFP) battery energy storage system," in *Proc. IEEE Energy Convers. Congr. Expo.*, 2012, pp. 3485–3492.

[12] B. Hredzak, V. G. Agelidis, and G. D. Demetriades, "A low complexity control system for a hybrid dc power source based on ultracapacitor-lead acid battery configuration," *IEEE Trans. Power Electron.*, vol. 29, no. 6, pp. 2882–2891, Jun. 2014.

[13] B. Hredzak, V. G. Agelidis, and J. Minsoo, "A model predictive control system for a hybrid battery-ultracapacitor power source," *IEEE Trans. Power Electron.*, vol. 29, no. 3, pp. 1469–1479, Mar. 2014.

[14] G. Lijun, R. A. Dougal, and S. Liu, "Power enhancement of an actively controlled battery/ultracapacitor hybrid," *IEEE Trans. Power Electron.*, vol. 20, no. 1, pp. 236–243, Jan. 2005.

[15] *Product Guide – Maxwell Technologies BOOSTCAP Ultracapacitors*, Maxwell Technologies, San Diego , CA, USA, 2009.

[16] J. Minsoo and V. G. Agelidis, "A minimum power-processing-stage fuel-cell energy system based on a boost-inverter with a bidirectional backup battery storage," *IEEE Trans. Power Electron.*, vol. 26, no. 5, pp. 1568–1577, May 2011.

[17] J. Minsoo, M. Ciobotaru, and V. G. Agelidis, "A single-phase grid-connected fuel cell system based on a boost-inverter," *IEEE Trans. Power Electron.*, vol. 28, no. 1, pp. 279–288, Jan. 2013.

[18] Z. Guo-Rong, T. Siew-Chong, C. Yu, and C. K. Tse, "Mitigation of low-frequency current ripple in fuel-cell inverter systems through waveform control," *IEEE Trans. Power Electron.*, vol. 28, no. 2, pp. 779–792, Feb. 2013.

[19] Z. Guo-Rong, X. Cheng-Yuan, W. Hao-Ran, C. Wei, and T. Siew-Chong, "Dynamic characteristics of boost inverter with waveform control," in *Proc. 29th Annu. IEEE Appl. Power Electron. Conf. Expo.*, 2014, pp. 1771–1775.

[20] H. R. Wang, G. R. Zhu, X. B. Fu, W. X. Liu, C. Y. Xiao, B. Liang, and S. C. Tan, "Mitigating low frequency ripple in multiply micro sources inverter system with waveform control method," in *Proc. IEEE 23rd Int. Symp. Ind. Electron.*, 2014, pp. 2390–2394.

[21] D. B. W. Abeywardana, B. Hredzak, and V. G. Agelidis, "A Rule-based Controller to Mitigate DC-Side 2nd-Order Harmonic Current in a Single-Phase Boost Inverter," *IEEE Trans. Power Electron.*, vol.PP, no.99, pp.1–1, 2014.

[22] W. Jianhua, J. Baojian, L. Xuqian, D. Xiang, Z. Fanghua, and G. Chunying, "Steady-State and dynamic input current low-frequency ripple evaluation and reduction in two-stage single-phase inverters with back current gain model," *IEEE Trans. Power Electron.*, vol. 29, no. 8, pp. 4247–4260, Aug. 2014.

[23] L. Changrong and L. Jih-Sheng, "Low frequency current ripple reduction technique with active control in a fuel cell power system with inverter load," *IEEE Trans. Power Electron.*, vol. 22, no. 4, pp. 1429–1436, Jul. 2007.

[24] T. Yi and F. Blaabjerg, "A component-minimized single-phase active power decoupling circuit with reduced current stress to semiconductor switches," *IEEE Trans. Power Electron.*, vol. 30, no. 6, pp. 2905–2910, Jun. 2015.

[25] Y. Tang, Z. Qin, F. Blaabjerg, and P. C. Loh, "A dual voltage control strategy for single-phase PWM converters with power decoupling function," *IEEE Trans. Power Electron.*, vol. 30, no. 12, pp. 7060–7071, Dec. 2015.

[26] Z. Qing-Chang, M. Wen-Long, C. Xin, and M. Krstic, "Reduction of DC-bus voltage ripples and capacitors for single-phase PWM-controlled rectifiers," in *Proc. 38th Annu. Conf. IEEE Ind. Electron. Soc.*, 2012, pp. 708–713.

[27] T. Yi, F. Blaabjerg, L. P. Chiang, J. Chi, and W. Peng, "Decoupling of fluctuating power in single-phase systems through a symmetrical half-bridge circuit," *IEEE Trans. Power Electron.*, vol. 30, no. 4, pp. 1855–1865, Apr. 2015.

[28] R. Teodorescu, M. Liserre, and P. Rodríguez, *Grid Converters for Photovoltaic and Wind Power Systems*. Hoboken, NJ, USA: Wiley, 2011.

[29] D. B. W. Abeywardana, B. Hredzak, and V. G. Agelidis, "A single phase grid integration scheme for battery-supercapacitor AC line hybrid storage system," in *Proc. IEEE Int. Conf. Ind. Technol.*, 2014, pp. 235–240.

[30] D. B. W. Abeywardana, B. Hredzak, and V. G. Agelidis, "Single-phase grid-connected lifepo4 battery-supercapacitor hybrid energy storage system with interleaved boost inverter," *IEEE Trans. Power Electron.*, vol. 30, no. 10, pp. 5591–5604, Oct. 2015.

[31] M. Ciobotaru, V. G. Agelidis, R. Teodorescu, and F. Blaabjerg, "Accurate and less-disturbing active antiislanding method based on PLL for grid-connected converters," *IEEE Trans. Power Electron.*, vol. 25, no. 6, pp. 1576–1584, Jun. 2010.

Authors' photographs and biographies not available at the time of publication.